

Article

Low-Complexity Modulation Format Identification Based on Amplitude Histogram Distributions for Digital Coherent Receivers

Ming Hao ^{1,2,3,4}, Xuedong Jiang ¹, Xingzhong Xiong ^{1,2}, Roger Giddings ³, Wei He ¹ and Jianming Tang ^{3,*}

¹ School of Automation and Information Engineering, Sichuan University of Science and Engineering, Yibin 644000, China; haoming@suse.edu.cn (M.H.); 320085404108@stu.suse.edu.cn (X.J.); xzxiong@suse.edu.cn (X.X.); 321085404334@suse.edu.cn (W.H.)

² Artificial Intelligence Key Laboratory of Sichuan Province, Sichuan University of Science and Engineering, Yibin 644000, China

³ The DSP Centre of Excellence, School of Computer Science and Electronic Engineering, Bangor University, Bangor LL57 1UT, UK; r.p.giddings@bangor.ac.uk

⁴ Key Laboratory of Higher Education of Sichuan Province for Enterprise Informationalization and Internet of Things, Sichuan University of Science and Engineering, Yibin 644000, China

* Correspondence: j.tang@bangor.ac.uk

Abstract: In this work, a prior-training-free and low-complexity modulation format identification (MFI) scheme, based on amplitude histogram distributions, was proposed and demonstrated, both numerically and experimentally, for autonomous digital coherent receivers. In the proposed scheme, after having performed power normalization, incoming polarization division multiplexed (PDM) signals were classified into QPSK, 8QAM, 16QAM, 32QAM and 64QAM signals, according to their ratios. Ratios were defined according to specific features of their amplitude histograms. The proposed MFI scheme used only amplitude information. As such, it was insensitive to carrier phase noise. Furthermore, the proposed scheme did not require any prior information, such as optical signal-to-noise ratio (OSNR). The performance of the proposed MFI scheme was numerically verified using 28GBaud PDM-QPSK/-8QAM/-16QAM/-32QAM/-64QAM signals. The numerical simulation results showed that the proposed scheme was able to achieve a 100% correct identification rate for all five modulation formats when their OSNR values were higher than the thresholds corresponding to the 20% FEC correcting bit error rate (BER) of 2.4×10^{-2} . To further explore the effectiveness of the proposed MFI scheme, proof-of-concept experiments in 28GBaud PDM-QPSK/-8QAM/-16QAM, and 21.5GBaud PDM-32QAM transmission systems were also undertaken, which showed that the proposed scheme was robust against fiber nonlinearities. To explore the scheme's feasibility for use in practical transmission systems, the computational complexity analysis of the proposed scheme was conducted. It showed that, compared with relevant MFI schemes, the proposed MFI scheme was able to significantly reduce the computational complexity.

Keywords: modulation format identification; coherent optical communications; amplitude histogram distributions



Citation: Hao, M.; Jiang, X.; Xiong, X.; Giddings, R.; He, W.; Tang, J.

Low-Complexity Modulation Format Identification Based on Amplitude Histogram Distributions for Digital Coherent Receivers. *Photonics* **2023**, *10*, 472. <https://doi.org/10.3390/photronics10040472>

Received: 22 February 2023

Revised: 6 April 2023

Accepted: 10 April 2023

Published: 20 April 2023



Copyright: © 2023 by the authors. Licensee MDPI, Basel, Switzerland. This article is an open access article distributed under the terms and conditions of the Creative Commons Attribution (CC BY) license (<https://creativecommons.org/licenses/by/4.0/>).

1. Introduction

To meet the growing demand for support for diverse data services, such as the Internet of Things, Big Data, cloud computing and video streaming, spectrum-sliced elastic optical networks (EONs) [1] were proposed. These have attracted considerable interest from the telecommunications R&D community worldwide [2]. A key focal point has been addressing the developing trend, in optical networks, of evolving from fixed network architectures to flexible and elastic ones [3,4]. According to different transmission link conditions and various quality of service requirements, transceivers involved in EONs have to be capable of dynamically adjusting their operation parameters—including, for example, modulation formats, symbol rates and transmission power—in order to maximize

their signal transmission capacities and spectral/power utilization efficiency. In traditional optical networks, these parameters are delivered to the corresponding receivers by the supervisory control layer of the optical networks. However, if the supervisory channel is disrupted and/or does not respond to the dynamic traffic demands with sufficient speed, the digital coherent receivers may fail to work appropriately [5–7]. In addition, both the cross-layer communications and end-to-end handshaking have been regarded as major factors limiting the flexibility of next-generation optical networks. Therefore, it is highly desirable that digital coherent receivers be able to autonomously identify these transmission parameters without assistance from the supervisory control layer.

Of the aforementioned parameters, the modulation format is one of the most important. It is crucial to identify and monitor the modulation format in real time in communication scenarios with timing-varying channel characteristics, where adaptive signal modulation format variations must be implemented. The use of MFI techniques would eliminate the transmissions of signal modulation format information between the transceivers, thus considerably reducing unwanted overhead. The MFI algorithm could be applied before modulation format-dependent algorithms, including polarization demultiplexing, frequency offset compensation and carrier phase recovery [8], ensuring optimal system performance.

The previously-reported MFI schemes for optical fiber communications were roughly classified into the following three categories: (1) data-aided schemes [9–11], in which additional pilot information is introduced and the computational complexity of the MFI scheme is low (at the cost of reduced spectral efficiency); (2) schemes based on Stokes space [7,8,12–23], which are not sensitive to carrier phase noise, frequency offset or polarization mixing; (3) schemes based on signal characteristics arising from constant modulus algorithm (CMA) equalization [24–33], which are based on CMA-equalized signals and do not require any space mapping. Meanwhile, CMA can also compensate for residual chromatic dispersion (CD) and polarization mode dispersion (PMD). However, these schemes face a significant challenge, in that modulation format features are ambiguous under the effects of noise and other transmission impairments. In recent years, due to the power of ambiguous information identification, machine learning technologies have been widely employed for the identification of CMA equalized signals. These have included convolutional neural networks (CNN) [2], binarized neural networks (BNN) [3], support vector machine learning (SVM) [5], random forest methods [6], and deep neural networks (DNN) [34,35]. Assisted by the powerful properties of machine learning, these schemes have been able to achieve high MFI performances. However, in order to obtain the desired optimal performances, these schemes require a large number of training samples, high computational resources and a complex training process. Meanwhile, if link conditions, such as distance, or other parameters change, machine learning models may need to be retrained [29]. Therefore, a prior-training-free and low-complexity MFI scheme is highly desirable for practical deployment.

In this paper, a prior-training-free MFI scheme, based on amplitude histogram distributions, was proposed for autonomous digital coherent receivers. Since there are different amplitude levels for QPSK, 8QAM, 16QAM, 32QAM and 64QAM, the amplitude histograms of CMA-equalized signals were applied to extract key features required for identification of different modulation formats. The proposed scheme mainly focused on identifying effective local features of amplitude histograms, rather than global features [6,20,34,36]. In the proposed MFI scheme, after having normalized the signal power, the ratios of specific parts of the amplitude histograms were calculated, based on which five modulation formats could be identified. The proposed scheme did not require any prior-training or information, such as OSNR, and was also insensitive to carrier phase noise. The performance of the proposed MFI scheme was first explored by numerical simulation, using 28GBaud PDM-QPSK/-8QAM/-16QAM/-32QAM/-64QAM signals. The simulation results showed that the proposed scheme was able to achieve 100% of the correct MFI rate for all five modulation formats when the OSNR values were higher than their corresponding theoretical 20% forward error correction (FEC) limit ($\text{BER} = 2.4 \times 10^{-2}$). For 28GBaud

PDM-QPSK/-8QAM/-16QAM, and 21.5GBaud PDM-32QAM systems subject to back-to-back and long-haul fiber transmission link conditions, proof-of-concept experiments were undertaken to further verify the effectiveness of the proposed MFI scheme. The experimental results showed that the proposed scheme was robust against fiber nonlinearities and suitable for use in long-haul transmission links. Finally, the computational complexity of the proposed scheme was also discussed. It was considerably lower than relevant MFI schemes. The proposed scheme demonstrated a good tradeoff between identification performance and computational complexity, and could therefore be regarded as a good candidate for use in EONs with improved flexibility.

2. Operating Principle

The digital signal processing (DSP) procedure of the autonomous digital coherent receiver considered herein is depicted in Figure 1, where the proposed MFI scheme has been highlighted. Before conducting the MFI operation, modulation format-independent algorithms (shown in the purple area) were employed to compensate for the CD impairments and timing-jitter and to achieve preliminary polarization demultiplexing. It should be noted that m PSK signals can be completely polarization-demultiplexed by CMA. CMA is also capable of compensating residual CD and PMD for different modulation formats [2,5,28,31]. However, for m QAM ($m > 4$) signals, further polarization demultiplexing algorithms may also be required. After having performed the modulation format-independent operations, the proposed MFI scheme could then be applied. Its outputs were provided to the subsequent modulation format-dependent algorithms (shown in the pink box), which consisted of the multi-modulus algorithm (MMA), frequency offset compensation and carrier phase recovery to compensate for various transmission impairments experienced by the signals.

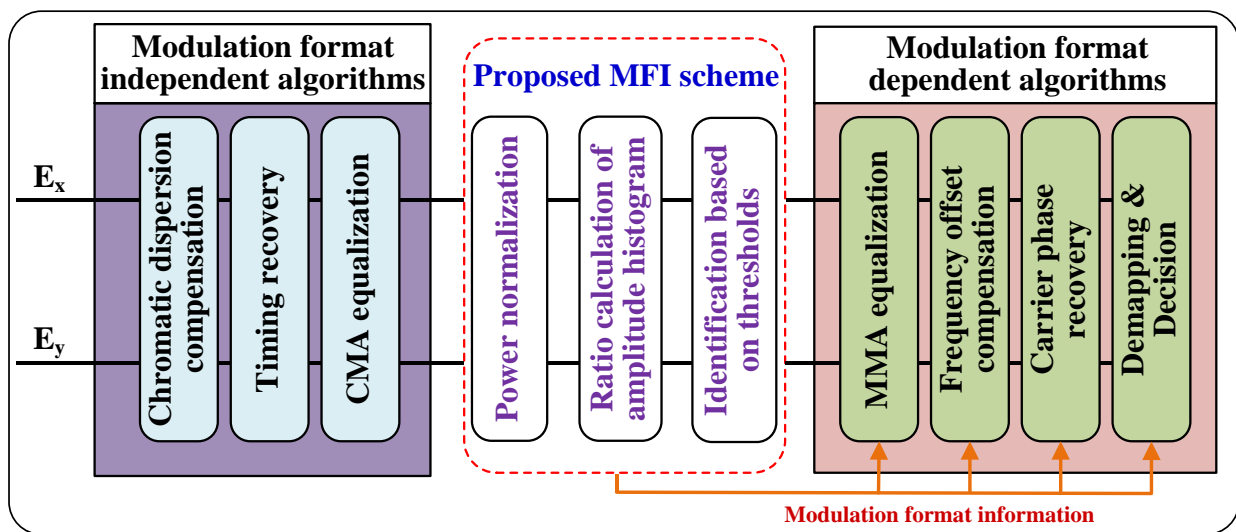


Figure 1. The DSP architecture with the proposed MFI scheme for autonomous digital coherent receivers.

As illustrated in Figure 1, the proposed MFI scheme consisted of three steps: first, the CMA equalized signals were power normalized. Then, the amplitude histograms of the signals were obtained, and calculations of the ratios (defined below) were subsequently undertaken. It should be noted that CMA-equalized signals of only one polarization were required to acquire the amplitude histogram. Finally, based on the thresholds of the ratios H_1, H_2, H_3 and H_4 , five commonly-adopted modulation formats, including PDM-QPSK/-8QAM/-16QAM/-32QAM/-64QAM, were identified.

As shown in Figure 2, there were one, two, three, five, and nine amplitude levels for QPSK, 8QAM, 16QAM, 32QAM, and 64QAM, respectively. For each level of these five modulation formats, the amplitude value and its associated probability are presented in

Table 1. Without loss of generality, the symbols of each modulation format were assumed to have a unit average power [37]:

$$\sum_{n=1}^m p_n \cdot Z_n^2 = 1 \tag{1}$$

where Z_n is the amplitude value, p_n is the associated probability for the n -th level, and m is the number of total levels for the considered modulation format. The amplitude levels of the different modulation formats can be clearly seen in Figure 2. However, in practical transmission systems, the distributions of the amplitude levels may be indistinct, even if CD, timing-jitter, and partial polarization mixing are compensated for using the modulation format independent algorithms. As such, it could be difficult to identify high-order modulation formats, especially in low OSNR cases. To address this challenge, the amplitude histogram of the CMA-equalized signals was employed to identify these five modulation formats over a considerably widened OSNR range.

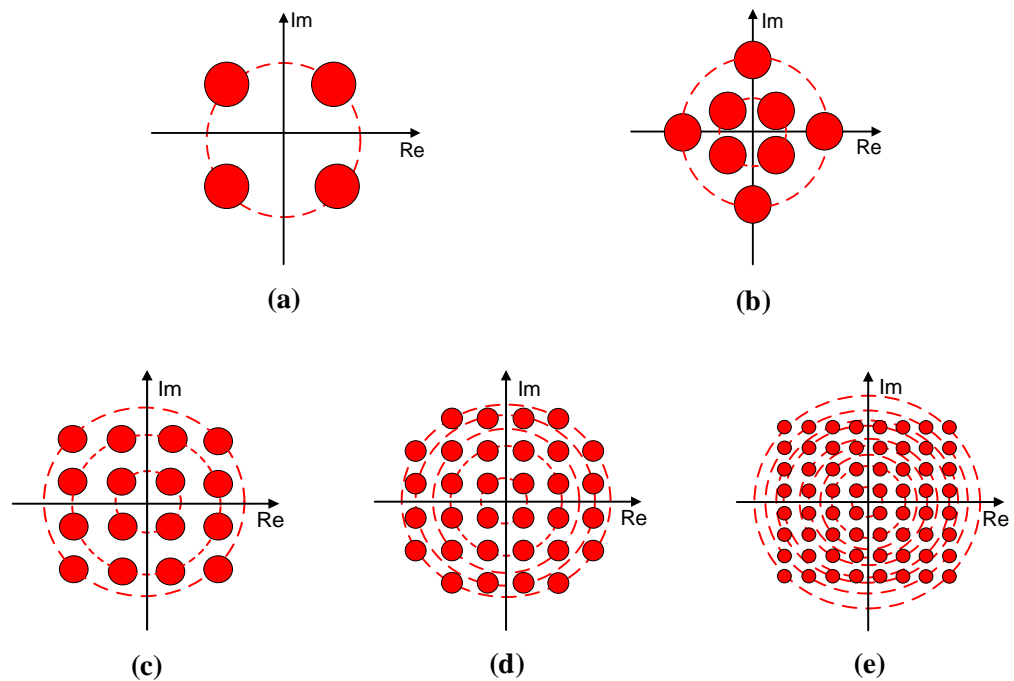


Figure 2. Constellation diagrams of five widely-employed modulation formats: (a) QPSK, (b) 8QAM, (c) 16QAM, (d) 32QAM and (e) 64QAM. There are one, two, three, five and nine amplitude levels for QPSK, 8QAM, 16QAM, 32QAM and 64QAM, respectively.

Table 1. Amplitude value and associated probability for each level of the five modulation formats.

QPSK	8QAM	16QAM	32QAM	64QAM
				0.218/6.25%
				0.488/12.5%
			0.316/12.5%	0.655/6.25%
		0.447/25%	0.707/25%	0.787/12.5%
1/100%	0.577/50%	1/50%	0.949/12.5%	0.900/12.5%
	1.291/50%	1.342/25%	1.140/25%	1.091/18.75%
			1.304/25%	1.175/12.5%
				1.327/12.5%
				1.528/6.25%

The amplitude histograms of these five modulation formats are shown in Figure 3, where the OSNR values for the PDM-QPSK/-8QAM/-16QAM/-32QAM/-64QAM signals

were fixed at 13 dB, 18 dB, 20 dB, 24 dB and 25 dB, respectively. For all of the amplitude histograms illustrated in Figure 3, the total number of symbols N was 6000. The same N value was also utilized, as shown in Figures 4 and 5, and the bin number of all of the amplitude histograms was 40. The first partition operation was employed for the sake of separation between 8QAM and four other modulation formats. The amplitude histograms were divided into two parts based on the number of symbols, which was $N/2$ in both part A and B. Since 8QAM included two amplitude levels, as mentioned in Table 1, the signal amplitudes for part A concentrated around 0.577 while, for part B, the amplitudes concentrated around 1.291, even in the presence of noise. In other words, the average signal amplitude for part B was approximately doubled, compared to part A. The corresponding ratio for the 8QAM signals was the largest among the five modulation formats. In this case, the ratio H_1 was defined as

$$H_1 = \frac{H_{B1}}{H_{A1}} \tag{2}$$

where:

$$H_{A1} = m_1 \times c_1 + \dots + m_i \times c_i + \left(\frac{N}{2} - \sum_{x=1}^i m_x\right) \times c_{i+1}$$

$$H_{B1} = \left(\sum_{x=1}^{i+1} m_x - \frac{N}{2}\right) \times c_{i+1} + m_{i+2} \times c_{i+2} + \dots + m_{nbins} \times c_{nbins}$$

$$\sum_{x=1}^i m_x \leq \frac{N}{2},$$

$\sum_{x=1}^{i+1} m_x > \frac{N}{2}$. m_i denotes the number of symbols in the i -th bin, c_i represents the central amplitude value of the i -th bin, N indicates the total number of symbols and $nbins$ is the total number of bins. In order to accurately divide the amplitude histogram into two parts, the symbols in the $i + 1$ bin were divided into two different parts, $\frac{N}{2} - \sum_{x=1}^i m_x$ symbols were divided into part A and $\sum_{x=1}^{i+1} m_x - \frac{N}{2}$ symbols were divided into part B.

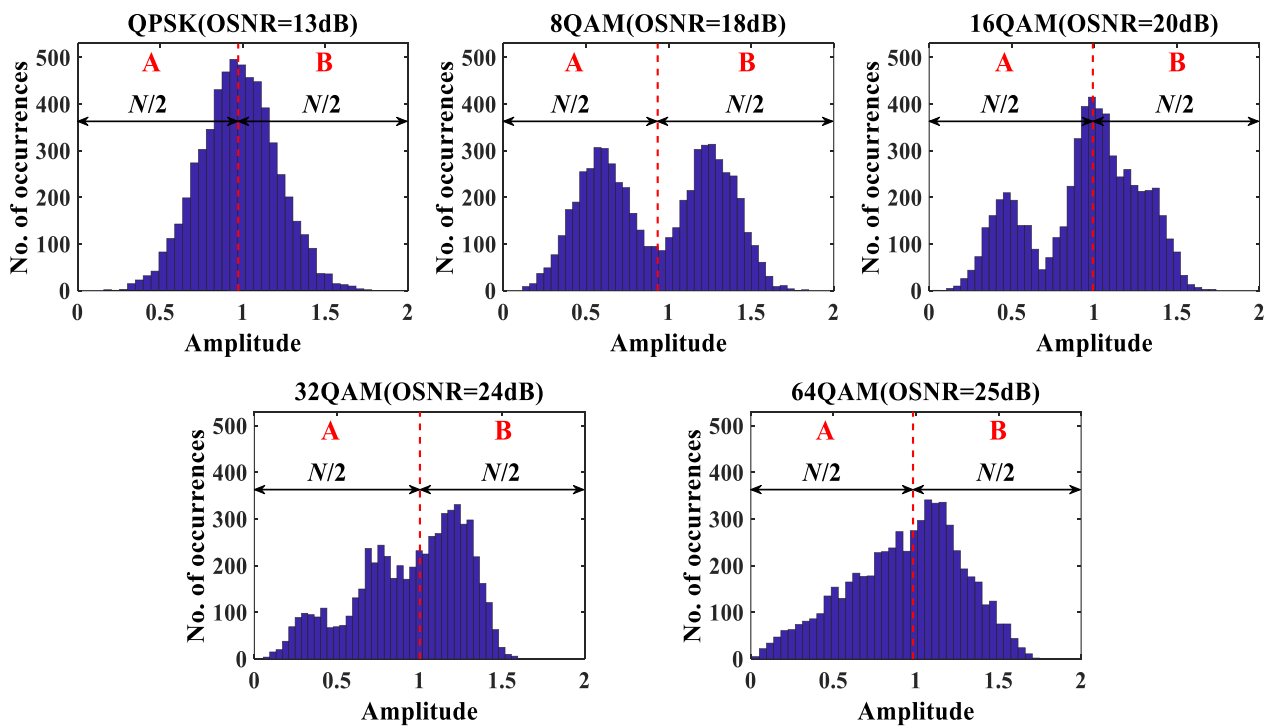


Figure 3. The first partition operation for the amplitude histograms of QPSK, 8QAM, 16QAM, 32QAM and 64QAM. The amplitude histograms are divided into two parts based on the number of symbols, which is $N/2$ in both part A and part B.

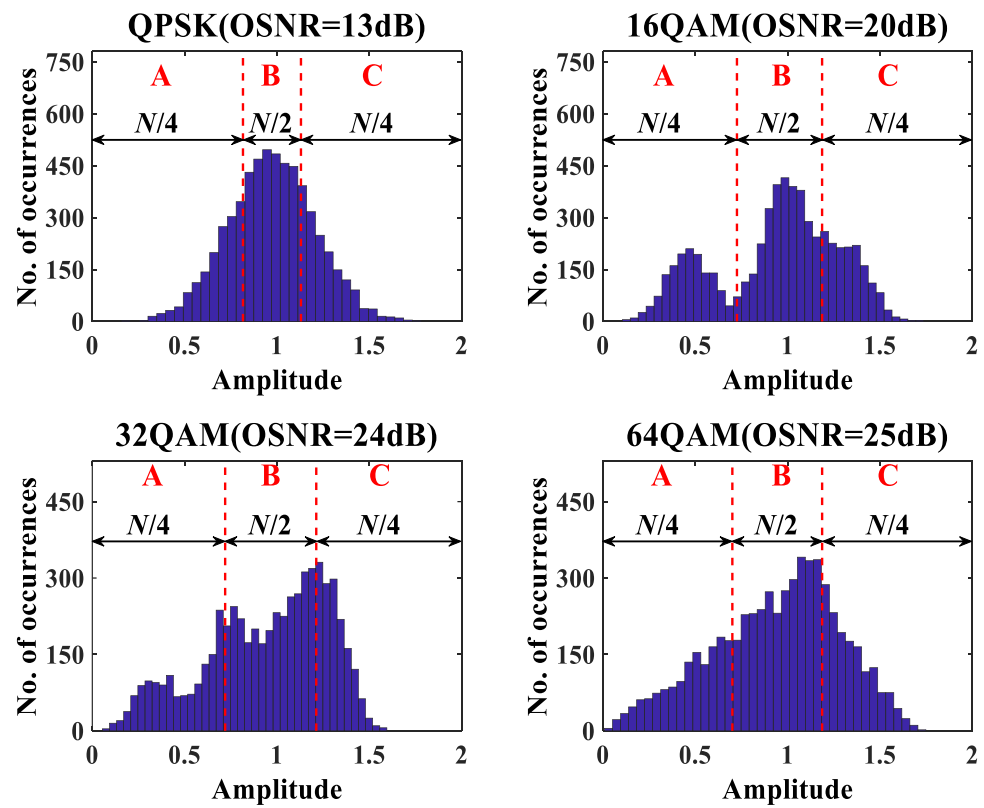


Figure 4. The second partition operation for the amplitude histograms of QPSK, 16QAM, 32QAM and 64QAM. The amplitude histograms of the four modulation formats are divided into part A, B and C. The number of symbols in part A, B and C are $N/4$, $N/2$ and $N/4$, respectively.

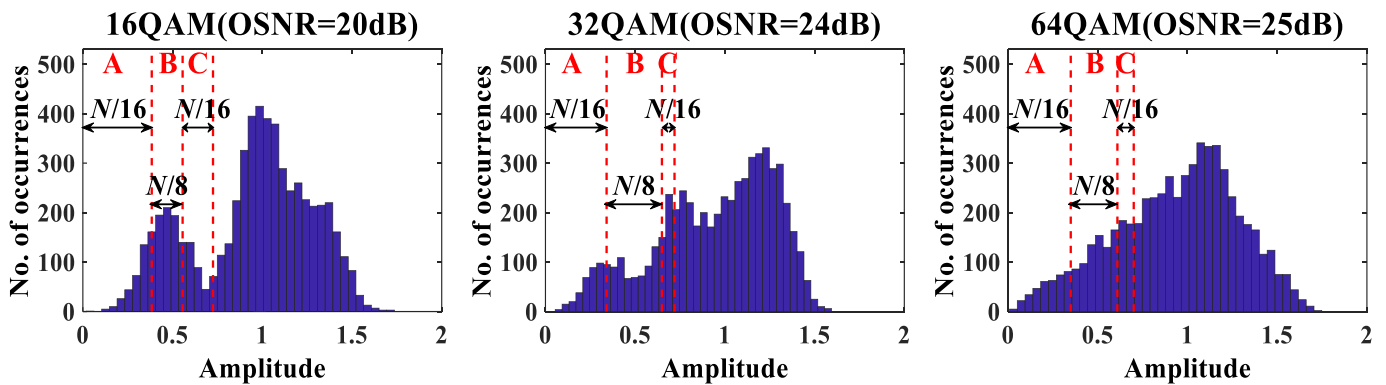


Figure 5. The third partition for the amplitude histograms of 16QAM, 32QAM and 64QAM. The first $N/4$ symbols are divided into three parts. The numbers of the symbols in part A, B and C are $N/16$, $N/8$ and $N/16$, respectively.

Since 8QAM could be distinguished based on the ratio H_1 , the purpose of the second partition operation was to identify QPSK from other three modulation formats. As shown in Figure 4, the amplitude histograms of the remaining four modulation formats were divided into parts A, B and C. The numbers of the symbols in parts A, B and C were $N/4$, $N/2$ and $N/4$, respectively. Due to the constant amplitude, the distribution of amplitudes for QPSK still concentrated around 1, even in the presence of noise. As a result, compared with the three other modulation formats, the amplitude distribution of the QPSK signals in part A and C was much closer. However, because of the influence of noise, such a distribution feature gradually grew less obvious for low OSNR cases. To address this

problem, we conducted a square operation of the number of symbols in each individual bin, and the corresponding ratio H_2 was defined as

$$H_2 = \frac{H_{C2}}{H_{A2}} \tag{3}$$

where

$$H_{A2} = m_1^2 \times c_1 + \dots + m_i^2 \times c_i + \left(\frac{N}{4} - \sum_{x=1}^i m_x\right)^2 \times c_{i+1}$$

$$H_{C2} = \left(\sum_{x=1}^{j+1} m_x - \frac{3N}{4}\right)^2 \times c_{j+1} + m_{j+2}^2 \times c_{j+2} + \dots + m_{nbins}^2 \times c_{nbins}$$

$$\sum_{x=1}^i m_x \leq \frac{N}{4}, \sum_{x=1}^{i+1} m_x > \frac{N}{4}$$

$$\sum_{x=1}^j m_x \leq \frac{3N}{4}, \sum_{x=1}^{j+1} m_x > \frac{3N}{4}$$

Due to the closer amplitude distributions of parts A and C, the ratio H_2 for QPSK was smaller than those of the three remaining modulation formats. Thus, QPSK could be identified. After that, the partition of the amplitude histogram remained unchanged. The difference was that only part B and C were taken into consideration. The ratio H_3 was introduced, calculated as

$$H_3 = \frac{H_{B3}}{H_{C3}} \tag{4}$$

where $H_{B3} = \left(\sum_{x=1}^{i+1} m_x - \frac{N}{4}\right)^2 \times c_{i+1} + m_{i+2}^2 \times c_{i+2} + \dots + \left(\frac{3N}{4} - \sum_{x=1}^j m_x\right)^2 \times c_{j+1}, \sum_{x=1}^i m_x \leq \frac{N}{4}, \sum_{x=1}^{i+1} m_x > \frac{N}{4}, \sum_{x=1}^j m_x \leq \frac{3N}{4}, \sum_{x=1}^{j+1} m_x > \frac{3N}{4}, H_{C3} = H_{C2}.$

Due to the square operation of the number of symbols in each bin, the distributions in part B and/or part C were more concentrated. Thus, the values of H_{B3} and/or H_{C3} were greater. As shown clearly in Table 1, for 32QAM, all of the symbols in part C concentrated around the fifth amplitude level, while the symbols in part B spread over three different amplitude levels. Thus, the ratio H_3 for 32QAM was small. Unlike 32QAM, the symbols for 64QAM, in part C, spread over three different amplitude levels. H_{C3} of 64QAM was much smaller than that of 32QAM. For 16QAM, the symbols in part B and part C were concentrated around the second and third amplitude levels, respectively. H_{B3} of 16QAM was much greater than that of 32QAM. Without considering noise and/or any other transmission impairments, the theoretical values of H_3 for 16QAM, 32QAM and 64QAM were 2.98, 1.19 and 2.21, respectively. Nevertheless, as the effects of noise increased for the low OSNR cases, the symbols of 32QAM in part C were dispersed, which resulted in an increased value of H_3 . Incorrect decisions could thus be made between H_3 of 16QAM for high OSNR cases and H_3 of 32QAM for low OSNR cases. Therefore, while relying solely on a single ratio H_3 , one could not accurately distinguish 32QAM from 16QAM over a wide OSNR range. To address this problem, an additional ratio was also required, as detailed below.

As seen in Figure 5, the third partition of the amplitude histogram divided the first $N/4$ symbols into three parts. The numbers of symbols in part A, B and C were $N/16$, $N/8$ and $N/16$, respectively. As listed in Table 1, the first $N/4$ symbols in the amplitude histogram corresponded to only one amplitude value for 16QAM, while the symbols for 32QAM and 64QAM corresponded to two and three amplitude values, respectively. Even under the effects of noise, for 16QAM, the distribution of amplitudes in part A and C still concentrated around 0.447. By comparison, the distributions of part A and C spread more widely for 32QAM and 64QAM. Therefore, the ratio H_4 was introduced and defined as

$$H_4 = \frac{H_{C4}}{H_{A4}} \tag{5}$$

$$H_{A4} = m_1 \times c_1 + \dots + m_i \times c_i + \left(\frac{N}{16} - \sum_{x=1}^i m_x\right) \times c_{i+1}$$

where

$$H_{C4} = \left(\sum_{x=1}^{j+1} m_x - \frac{3N}{16}\right) \times c_{j+1} + m_{j+2} \times c_{j+2} + \dots + \left(\frac{N}{4} - \sum_{x=1}^k m_x\right) \times c_{k+1}$$

$$\sum_{x=1}^i m_x \leq \frac{N}{16}, \sum_{x=1}^{i+1} m_x > \frac{N}{16}$$

$$\sum_{x=1}^j m_x \leq \frac{3N}{16}, \sum_{x=1}^{j+1} m_x > \frac{3N}{16}, \sum_{x=1}^k m_x \leq \frac{N}{4}, \sum_{x=1}^{k+1} m_x > \frac{N}{4}$$

Due to the more concentrated distribution, H_{A4} of 16QAM was relatively larger than those related to 32QAM and 64QAM, while H_{C4} was relatively smaller than those related to 32QAM and 64QAM, resulting in a smaller H_4 . As a direct result, 16QAM and 32QAM could be identified over a wide OSNR range by making use of both H_3 and H_4 . Meanwhile, although 16QAM and 64QAM could be distinguished by relying on H_4 only, as seen in Figure 6, the utilization of both H_3 and H_4 was necessary for identifying 16QAM.

As mentioned above, the different modulation formats gave rise to different ratios. Figure 6 shows the values of H_1, H_2, H_3 and H_4 for the five modulation formats in different OSNR cases. The number of symbols was 6000, and the bin number of the amplitude histogram was 40. By selecting appropriate thresholds, the incoming PDM signals could be identified as QPSK, 8QAM, 16QAM, 32QAM or 64QAM signals. The corresponding thresholds of H_1, H_2, H_3 and H_4 were 1.984, 2.64, 2.02 and 2.4/2.637, respectively, as indicated by the dotted red lines in Figure 6. It should be noted that there were two thresholds of H_4 for distinguishing 16QAM from 32QAM (2.4) and 64QAM (2.637). The thresholds for H_1, H_2, H_3 and H_4 were determined to balance the optimal identification performance of each identified modulation format. Figure 7 illustrates a flow chart of the proposed MFI scheme. If H_1 of the incoming signals was greater than 1.984, the signals were recognized as 8QAM signals, otherwise, if H_2 of the incoming signals was less than 2.64, the signals were identified as QPSK signals. The remaining 16QAM, 32QAM and 64QAM signals could be further distinguished by making use of both H_3 and H_4 .

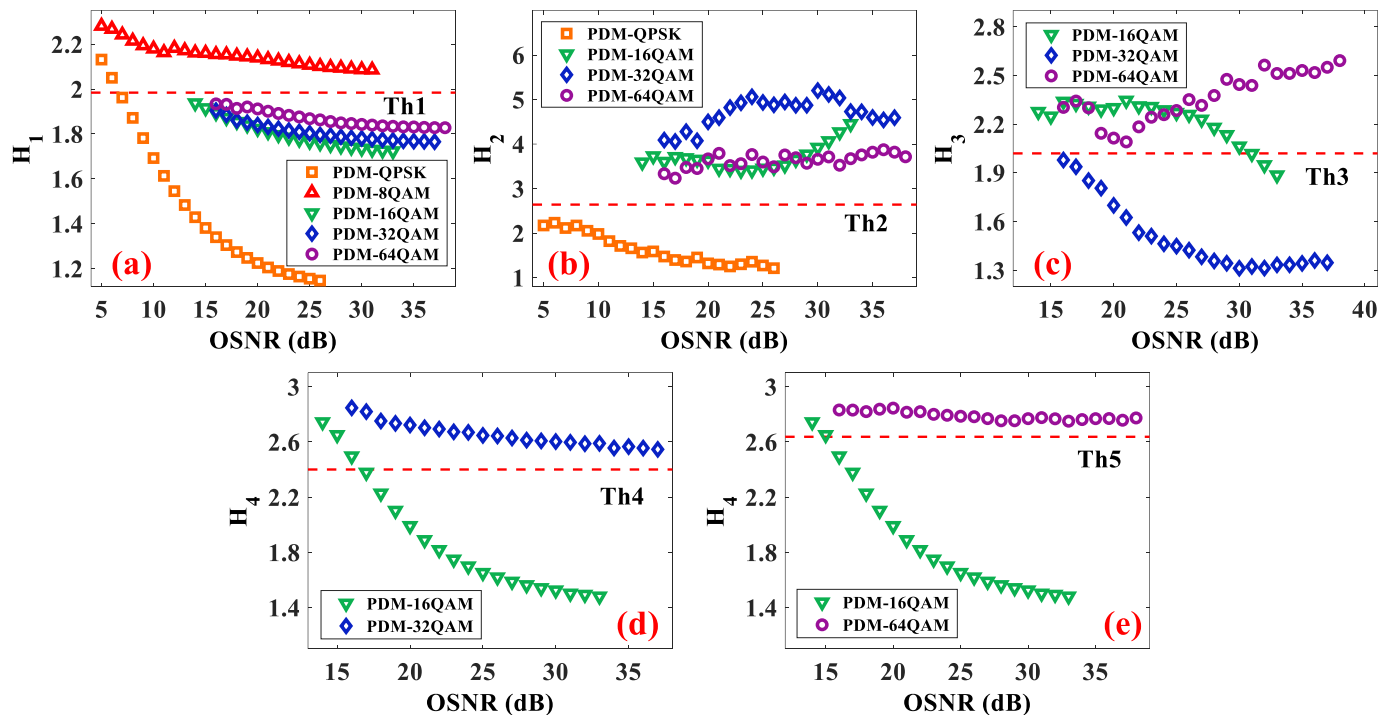


Figure 6. Ratios varies with OSNR in back-to-back simulation: (a) H_1 ; (b) H_2 ; (c) H_3 ; (d) H_4 (for separating 16QAM and 32QAM); (e) H_4 (for separating 16QAM and 64QAM). The dotted red lines indicate the corresponding thresholds.

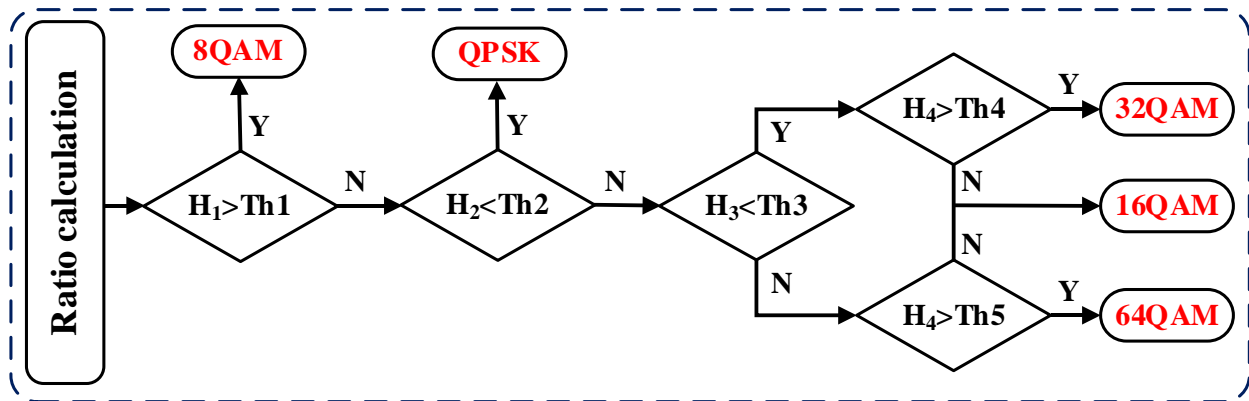


Figure 7. Flow chart of the proposed MFI scheme.

3. Numerical Simulation Results

VPI Transmission Maker 9.8 was utilized to undertake a series of numerical simulations and extensively verify the proposed MFI scheme. The length of the pseudo-random bit sequence (PRBS) was $2^{15} - 1$. Then, 28 GBaud PDM-QPSK/-8QAM/-16QAM/-32QAM/-64QAM signals were generated in the transmitter. The sample rate was 56 GSa/s, and the roll-off factor of the square root raised cosine (SRRC) filter was 0.1. The wavelength and linewidth of the laser were 1550 nm and 100 kHz, respectively. The modulated signals were then passed through an additive Gaussian white noise (AWGN) channel with adjustable OSNRs, calculated at a 0.1 nm ASE noise bandwidth. These PDM signals were finally detected, and their modulation formats were identified by a coherent receiver utilizing an off-line DSP module based on the proposed MFI scheme, as shown in Figure 1. The OSNR ranges of the PDM-QPSK/-8QAM/-16QAM/-32QAM/-64QAM signals were 5–26 dB, 5–31 dB, 14–33 dB, 16–37 dB and 16–38 dB, respectively, with an OSNR incremental of 1 dB. In order to evaluate the performance of the proposed scheme, for each modulation format, 100 independent simulations were conducted for each OSNR value.

For an MFI scheme, the minimum required number of symbols (corresponding to the lowest OSNR required for the considered modulation format) is one of the most important factors, because it determines the response speed and computational complexity of the MFI algorithm [28,32]. The minimum required OSNR values, versus the numbers of symbols for the five modulation formats, are shown in Figure 8, wherein the symbol variation ranged from 1000 to 7000 at intervals of 1000. For QPSK, 8QAM, 16QAM and 32QAM, when the number of symbols was greater than or equal to 2000, the minimum required OSNR value to achieve a correct identification rate of 100% remained almost constant. Meanwhile, since 64QAM was the highest order of modulation format, with more amplitude levels, an efficient feature extraction required more symbols to be employed. If the number of symbols was lower than 6000, the minimum required OSNR value increased substantially. Since the required number of symbols for the proposed MFI scheme was determined by the highest order modulation format, the numbers of symbols for all of the considered modulation formats were set at 6000 in the following numerical simulations and proof-of-concept experiments. It should be noted that, when the number of symbols was lower than 2000 or 5000, for 8QAM or 64QAM respectively, a correct identification rate of 100% could not be obtained.

The number of histogram bins was another factor that determined the computational complexity of the proposed MFI scheme. Similar to the number of symbols, an optimal number of the histogram bin was also identified, as it gave rise to the minimum required OSNR value, as shown in Figure 9. If the number of histogram bins was less than 40, the minimum required OSNR values increased gradually, especially for 64QAM. As a result, in order to achieve an optimum tradeoff between computational complexity and MFI performance, the numbers of histogram bins for the five modulation formats were all taken to be 40 in the following numerical simulations and proof-of-concept experiments.

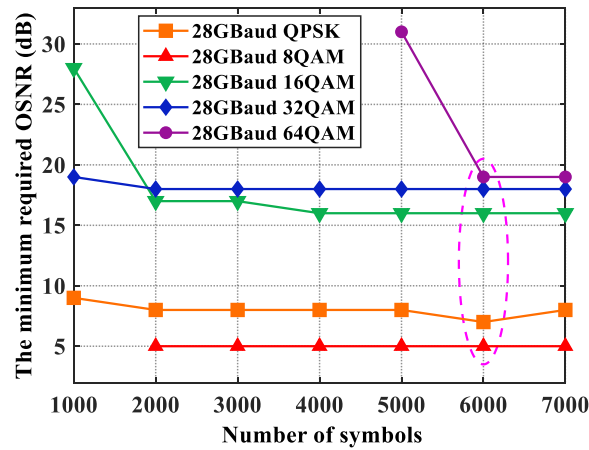


Figure 8. Minimum required OSNR values, with different numbers of symbols for five modulation formats; 6000 symbols is the optimum selection.

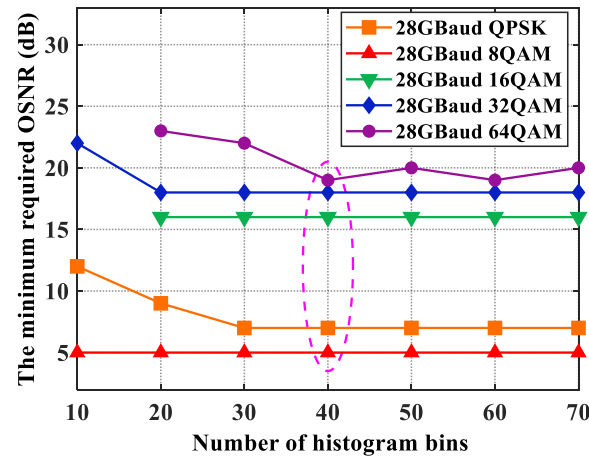


Figure 9. Minimum required OSNR values with different numbers of histogram bins for five modulation formats; 40 bins is the optimum selection.

In order to analyze the influence of carrier phase noise on the performance of the proposed MFI scheme, simulations (i.e., correct identification rate versus OSNR value under different linewidths) were undertaken, as shown in Figure 10a,b, respectively. Compared with Figure 10a, when the linewidth of the laser was 100 kHz, the constellation of 16QAM rotated, as shown in Figure 10b, due to the existence of carrier phase noise. However, since the amplitude histogram depended on amplitude information only, the effect of carrier phase noise on the amplitude histogram was almost negligible. Therefore, as shown in Figure 10a,b, when the value of the linewidth was increased from 0Hz to 100 kHz, the minimum required OSNR values to achieve a correct identification rate of 100% for the five modulation formats remained unchanged. In conclusion, the proposed MFI scheme was insensitive to carrier phase noise.

To explore the OSNR-dependent correct identification performance rates of the proposed MFI scheme under typical values of linewidth, for different signal modulation formats, their numerically-simulated correct identification rates, as a function of OSNR, are shown in Figure 10b. The simulation results showed that 100% accurate identification could be obtained for 8QAM even when the OSNR values were very low (5 dB). For QPSK, 16QAM, 32QAM and 64QAM, the minimum OSNR values for achieving the correct identification rate of 100% were 7 dB, 16 dB, 18 dB and 19 dB, respectively. As seen in Figure 10b, the proposed MFI scheme achieved a correct identification rate of 100% for all five modulation formats when the OSNR values were higher than their thresholds (indicated by vertical dash lines), corresponding to 20% FEC correcting BER of 2.4×10^{-2} .

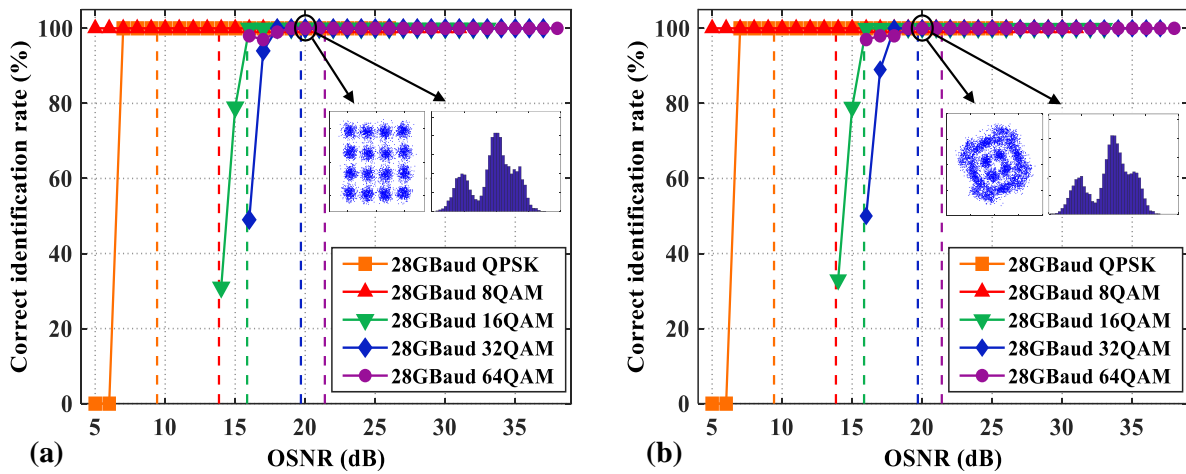


Figure 10. Simulation results of correct identification rate versus OSNR value under different linewidths: (a) 0 Hz; (b) 100 kHz. The illustrations are the constellation diagrams and amplitude histograms of PDM-16QAM when the linewidth is 0 Hz or 100 kHz, respectively. The vertical dash lines indicate the OSNR thresholds, corresponding to 20% FEC correcting BER of 2.4×10^{-2} .

By making use of incoming signals identical to those presented above, the performance of the proposed scheme was further evaluated in comparison with schemes using DNN, SVM, modified particle swarm optimization (M-PSO) [20] and principal component analysis of Stokes parameters (PCASP) [8]. The SVM and DNN schemes also adopted the amplitude histogram as the proposed scheme. The numbers of symbols and histogram bins were fixed at 6000 and 40, respectively. To ensure the optimal performance, a large training data set for DNN was required. The training set comprised 9200 ($18 \times 100 + 23 \times 100 + 15 \times 100 + 17 \times 100 + 19 \times 100$) amplitude histograms. In this work, a four-layer DNN was employed, in which the number of neurons in the input, first hidden, second hidden and output layer were 40, 40, 10 and 5, respectively. The activation functions of the hidden layer and output layer were *ReLU* and *softmax*, respectively [6]. On the other hand, since the complexity of SVM was related to the number of support vectors, by considering the tradeoff between the identification performance and the computational complexity for SVM, the training set of SVM comprised 3640 ($18 \times 40 + 23 \times 40 + 15 \times 40 + 17 \times 40 + 18 \times 40$) amplitude histograms. For SVM, the kernel function was the default radial basis function (RBF) kernel [38].

The minimum required OSNR comparisons between the proposed scheme and these four schemes are shown in Figure 11. The scheme based on M-PSO only identified three modulation formats, including QPSK, 8QAM and 16QAM, and the minimum required OSNR for identifying QPSK and 8QAM was much higher than that of the proposed scheme. The minimum required OSNRs of the proposed scheme, in order to identify each modulation format, were both lower than that of the schemes based on PCASP, except for 32QAM. For QPSK, 16QAM and 32QAM, the minimum required OSNR values for the proposed scheme were lower than those corresponding to DNN and SVM. For 8QAM and 64QAM, the proposed scheme offered minimum required OSNRs identical to DNN and SVM. The proposed scheme improved the performances because it primarily focused on identifying effective local features, while the MFI abilities of DNN and SVM came at the cost of higher complexity, focused on identifying global features. Furthermore, DNN and SVM also required more detailed amplitude histograms to complete the automatic feature extraction. Thus, 6000 symbols and 40 bins were not sufficient, giving rise to slower response speeds and increased computational complexity, as mentioned above.

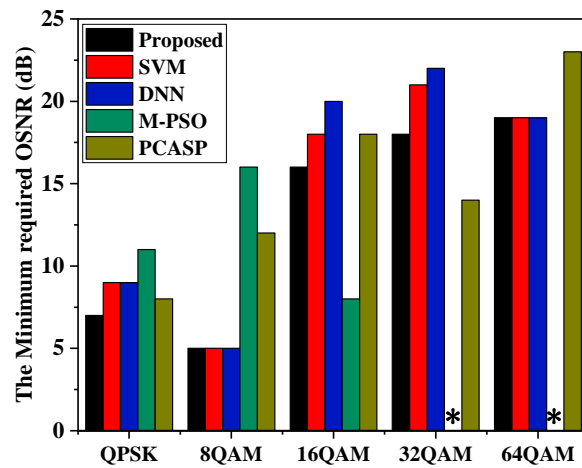


Figure 11. Minimum required OSNR for identifying different modulation formats for five MFI schemes. * indicates the modulation format is not identified by this scheme.

In order to evaluate the effects of residual CD and PMD on the identification performance of the proposed MFI scheme, numerical simulation was employed. It should be noted that, as shown in Figure 1, the proposed MFI scheme was placed after CMA equalization. The CMA could compensate residual CD and PMD. Therefore, the tolerance, with respect to residual CD and PMD of the proposed scheme, embedded in such DSP architecture, was enhanced. The tolerance values, with respect to residual CD and DGD of the proposed scheme, are shown in Figure 12a,b, respectively. The OSNR values of PDM-QPSK/-8QAM/-16QAM/-32QAM/-64QAM were 12 dB, 17 dB, 19 dB, 22 dB and 24 dB, respectively. The range of residual CD for PDM-QPSK/-8QAM/-16QAM/-32QAM signals was from -1920 ps/nm to 1920 ps/nm, while the range of residual CD for PDM-64QAM was -720 ps/nm~ 720 ps/nm. The steps for all modulation formats were 120 ps/nm. As shown in Figure 12a, the proposed MFI scheme was able to tolerate a relatively wide range of residual CDs for PDM-QPSK (-1920 ps/nm~ 1920 ps/nm), PDM-8QAM (-1920 ps/nm~ 1920 ps/nm), PDM-16QAM (-1440 ps/nm~ 1320 ps/nm) and PDM-32QAM (-1680 ps/nm~ 1680 ps/nm) signals. Because of the greater amplitude levels, for PDM-64QAM, the proposed scheme was able to tolerate residual CD from -240 ps/nm to 240 ps/nm.

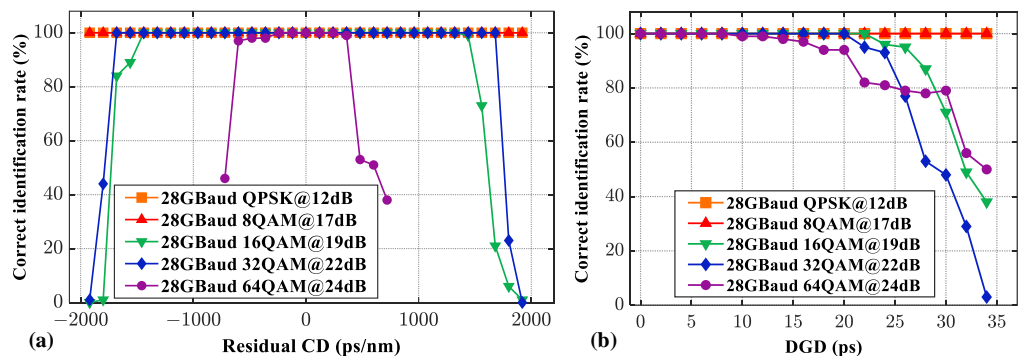


Figure 12. The tolerance with respect to (a) residual CD and (b) DGD of the proposed scheme.

The range of DGD for PDM-QPSK/-8QAM/-16QAM/-32QAM/-64QAM signals was from 0 ps to 34 ps, with a step size of 2 ps. Analogous to residual CD, the tolerable DGD for PDM-64QAM was much lower than the other four modulation formats. The proposed scheme was able to achieve a 100% correct identification rate for PDM-64QAM when the DGD was 8 ps. For PDM-16QAM and PDM-32QAM, the tolerable DGDs were 22 and 20 ps,

respectively. The correct identification rate of PDM-QPSK and PDM-8QAM remained at 100% over the whole DGD range.

In order to analyze the relationship between MFI performance and baud rate, *VPI Transmission Maker 9.8* was utilized to undertake numerical simulations for 10 GBaud and 20 GBaud transmission systems. The numerical simulation setup remained unchanged, except for baud rates. Simulated correct identification rates for the five modulation formats used in the 10 GBaud and 20 GBaud systems are shown in Figure 13a,b, respectively. These figures showed that, compared with the 28GBaud case, shown in Figure 10b, the MFI performances were relatively better because the tolerance to noise was improved for the lower baud rate cases.

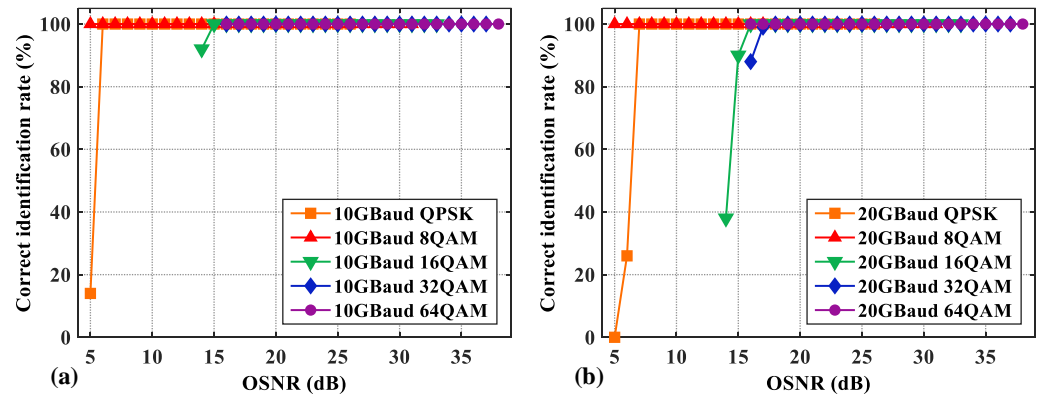


Figure 13. Simulation results of correct identification rate versus OSNR value, under different baud rate: (a) 10 GBaud; (b) 20 GBaud.

To discuss the scalability of the proposed scheme, the MFI performance for probabilistic shaping (PS) of QAM signals was also investigated. The amplitude value and associated probability values for each level of the PS-QAM signals, including PS-16QAM (3 bit/symbol) and PS-64QAM (5 bit/symbol), are shown in Table 2. Since the probability distribution feature of the PS-QAM signals differed from those of the traditional QAM signals, the procedure and corresponding thresholds of the proposed scheme needed to be modified accordingly, as detailed below.

Table 2. Amplitude value and associated probability for each level of PS-16QAM and PS-64QAM signals.

PS-16QAM (3 Bit/Symbol)		PS-64QAM (5 Bit/Symbol)	
Amplitude Value	Probability	Amplitude Value	Probability
0.731	79.40%	0.363	28.70%
		0.812	34.68%
		1.09	10.38%
1.634	19.40%	1.31	12.50%
		1.498	7.35%
		1.817	4.11%
		1.957	1.65%
2.193	1.20%	2.21	0.58%
		2.543	0.05%

The numerical simulation setup remained unchanged, except for the process used in generating the PS-16QAM and PS-64QAM signals. After power normalization, the first partition operations for the amplitude histograms of QPSK, 8QAM, PS-16QAM, 32QAM and PS-64QAM were employed. As shown in Figure 14a, the number of symbols was $N/2$

in both part A and part B. Since part A of PS-64QAM concentrated around low amplitude values (the associated probability for 0.363 was 28.7%), and the amplitude distribution range of part B as wide, as shown in Figure 14c, the ratio H_1 (mentioned in Equation (2)) of PS-64QAM was greater than that of 8QAM over a wide OSNR range. Therefore, two thresholds for H_1 were set: Th1 was 2.23 and Th2 was 2.04. Based on these two thresholds of H_1 , 8QAM as not only distinguishable from QPSK, PS-16QAM and 32QAM, but also from PS-64QAM. The second partition operation for the amplitude histograms of the rest of these modulation formats (QPSK, PS-16QAM and 32QAM) is shown in Figure 14b. The numbers of symbols in part A, part B and part C were $N/4$, $N/2$ and $N/4$, respectively. The distribution of PS-16QAM in part B was more concentrated than those of QPSK and 32QAM, while the distribution of PS-16QAM in part C was dispersed. Therefore, as shown in Figure 14d, the value of H_3 (mentioned in Equation (4)) for PS-16QAM was greater than those for QPSK and 32QAM. QPSK was also distinguishable from 32QAM based on another threshold of H_3 . The two thresholds of H_3 were 4.12 (Th3) and 2.3 (Th4). The correct identification rates for identifying QPSK, 8QAM, PS-16QAM, 32QAM and PS-64QAM are shown in Figure 14e. The proposed MFI scheme was still able to achieve a 100% correct identification rate for all of these five modulation formats over a wide OSNR range. The scalability of the proposed scheme was verified by the simulation results. It should also be noted that if the information entropy changed, the probability distribution features of PS-QAM also changed. As such, when PS-QAM (with different information entropy) needed to be identified, corresponding modifications needed to be made to the procedure of the proposed MFI scheme and their relevant thresholds. The proposed scheme was suitable for application scenarios wherein the set of the modulation formats that needed to be identified were made known before applying the MFI scheme.

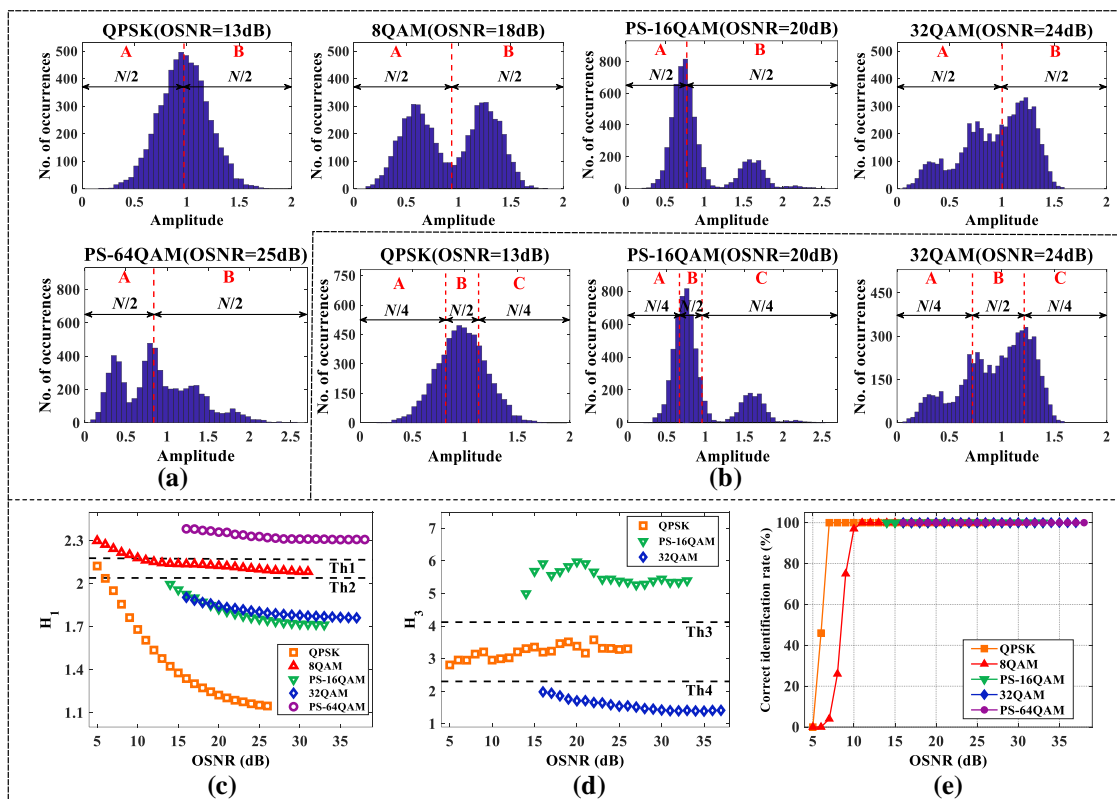


Figure 14. Operating principle and simulation results for identifying five modulation formats, including PS-QAM. (a) The first partition operation and (b) second partition operation for the amplitude histograms of QPSK, 8QAM, PS-16QAM, 32QAM and PS-64QAM; (c) H_1 and (d) H_3 vary with the OSNR of the back-to-back optical transmission system, and (e) the correct identification rate for identifying these five modulation formats.

4. Experimental Setup and Results

To experimentally verify the effectiveness of our proposed MFI scheme, a series of proof-of-concept experimental demonstrations were undertaken. The setup for these is shown in Figure 15. In the transmitter, a PRBS with a word length of $2^{15} - 1$ was generated by offline DSP and mapped onto different modulation formats with 2 samples/symbol. A SRRC filter with a roll-off factor of 0.1 was employed to shape the up-sampled signals. In addition, a pre-distortion operation was also applied to compensate for the frequency roll-off effect associated with digital-to-analog converters (DACs). An external cavity laser (ECL) produced a continuous wave optical carrier with a wavelength of ~ 1550 nm and a linewidth of ~ 100 kHz, which was then modulated by an integrated LiNbO₃ polarization-multiplexing I/Q modulator. The DACs, operating at 64 GSa/s and 25 GHz analog bandwidth, drove four branches of the modulator to generate 28 GBaud PDM-QPSK/-8QAM/-16QAM and 21.5 GBaud PDM-32QAM optical signals. The transmission links included back-to-back and long-haul fiber transmissions. The long-haul transmission link was composed of multi-span single mode fiber (SMF), whose dispersion parameter, attenuation, and nonlinear coefficient were $D = 16.9$ ps/nm/km, $\alpha = 0.2$ dB/km, and $\gamma = 1.27$ km⁻¹·W⁻¹, respectively. To completely compensate for the fiber loss, an erbium-doped fiber amplifier (EDFA) with a noise figure of ~ 5 dB was applied in each span. An optical spectrum analyzer (OSA ANRITSU MS9740A) was used before the receiver to measure the OSNR in back-to-back case, and an optical band-pass filter (OBPF), whose bandwidth was 200GHz, was employed to suppress out-of-band ASE noise. After passing through the link, the received signals were detected by an integrated coherent receiver and then sampled by a real-time digital oscilloscope with 80 GSa/s and 33 GHz electrical bandwidth. Finally, these signals were processed by an offline DSP module, where the proposed MFI scheme was embedded. The frame synchronization was achieved by the auto-correlation detection of synchronization codes. The OSNR dynamic ranges for PDM-QPSK/-8QAM/-16QAM/-32QAM signals in the back-to-back links were 10–17 dB, 15–28 dB, 16–28 dB and 18–35 dB, respectively. The step of variable OSNR is 1 dB. In all of the proof-of-concept experiments, 100 samples of independent data were applied for each OSNR or launch power value.

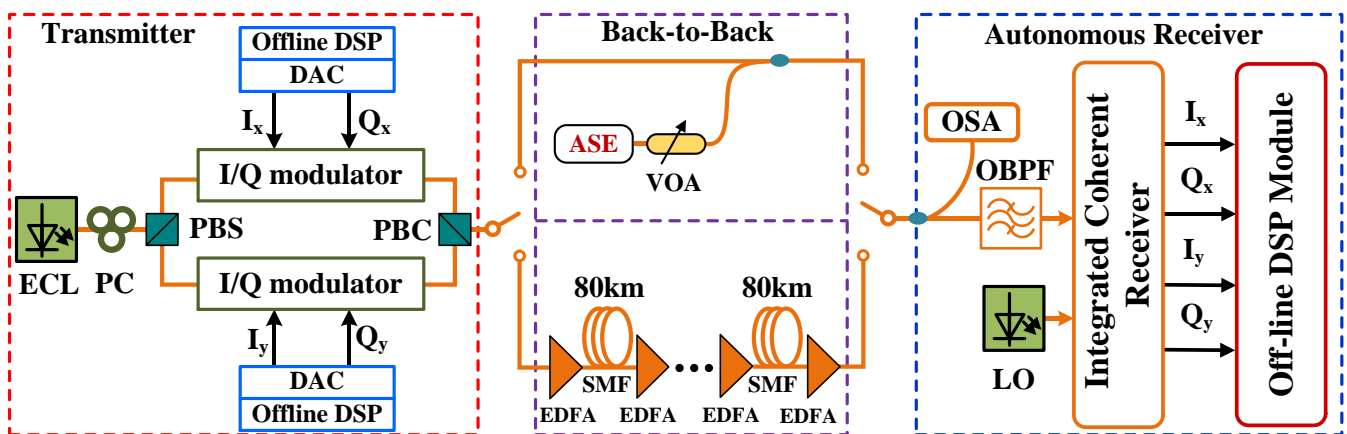


Figure 15. Proof-of-concept experimental setup of the proposed scheme. PC: polarization controller, PBS: polarization beam splitter, PBC: polarization beam coupler, VOA: variable optical attenuator, LO: local oscillator.

The performance of the proposed MFI scheme was first experimentally verified in back-to-back links. As shown in Figure 16, the proposed scheme achieved a 100% correct identification rate for both QPSK and 8QAM over all OSNR ranges considered in the experiments. The minimum OSNR values required by 16QAM and 32QAM for achieving a correct identification rate of 100% were 19 dB and 20 dB, respectively.

Compared with the numerical simulation results, the minimum required OSNR values for these two modulation formats increased slightly. This could have been due to the unwanted effects associated with the signal generation of high-order modulation formats in the experiments. The four modulation formats could still be identified with a 100% correct identification rate when their OSNR values were higher than the thresholds (indicated by the vertical dash lines), corresponding to the 7% FEC correcting BER of 3.8×10^{-3} .

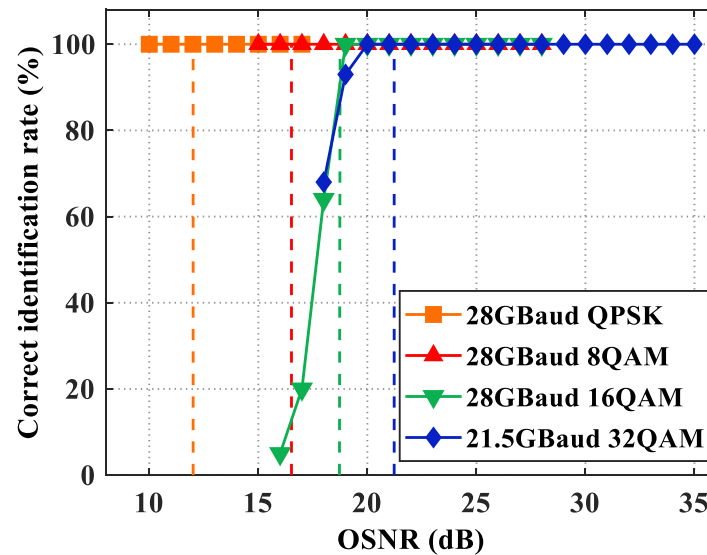


Figure 16. Correct identification rates under different OSNR values in back-to-back experiments. The vertical dash lines indicate the OSNR thresholds corresponding to 7% FEC correcting BER of 3.8×10^{-3} .

The performance of the proposed scheme, subject to nonlinear impairments of long-haul transmission links, was experimentally explored, and the results are presented in Figure 17. As shown, the launch powers of the PDM-QPSK signals over a 2000 km link, the PDM-8QAM signals over a 2000 km link, the PDM-16QAM signals over a 1040 km link and the PDM-32QAM signals over a 400 km link were varied in the ranges of $-4 \sim 6$ dBm, $-3 \sim 6$ dBm, $-3 \sim 8$ dBm, and $-2 \sim 7$ dBm, respectively. In Figure 17, EVM, as a function of launch power, was also plotted to evaluate the system’s overall performances with respect to different modulation formats. Note that, in comparison with other modulation formats, the EVM variation for 32QAM over the whole optical launch powers range was reduced because of the relatively short link length. As seen in the figure, when the launch power was higher than 2 dBm, all the transmission systems operated at the nonlinear region, where the system performance was dominated by fiber nonlinearity. Over such a region, the correct identification rates of 100% were still achievable for the four modulation formats. On the other hand, when launch powers were decreased to -4 dBm and -3 dBm for the PDM-QPSK and PDM-16QAM signals, respectively, as a direct result of the resulting reductions in OSNR, the correct identification rates for the PDM-QPSK and PDM-16QAM signals were reduced with decreasing launch power. The experiment results indicated that the proposed MFI scheme was robust against fiber nonlinearities and suitable for long-haul transmission links.

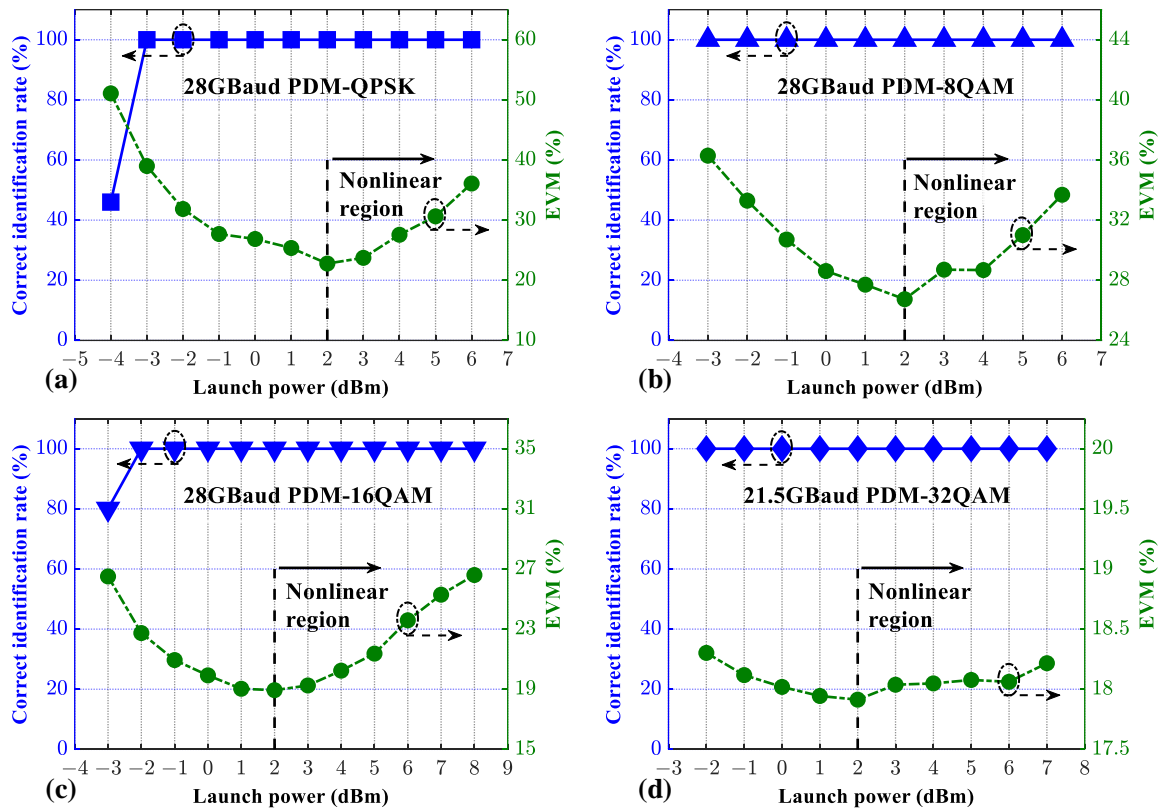


Figure 17. Correct identification rates (blue triangles) of the four modulation formats with different launch powers in long-haul transmission experiments. (a) PDM-QPSK signals over a 2000 km link; (b) PDM-8QAM signals over a 2000 km link; (c) PDM-16QAM signals over a 1040 km link; (d) PDM-32QAM signals over a 400 km link. Green dots indicate the error vector magnitudes (EVM).

5. Complexity Analysis

To evaluate the feasibility of the proposed MFI algorithm for use in practical systems, its computational complexity had to be examined. The detailed complexity analysis of the proposed scheme was thus undertaken. The results are presented in Table 3, where the complexities of the five operations involved in the proposed MFI scheme are shown. For the proposed scheme, the required real multipliers, real adders and comparators were $N + 6 \times (nbins + 1)$, $N + 7 \times nbins + 6$ and $2 \times N + (2 \times N + 10) \times nbins + 1$, respectively; here, N is the number of symbols (6000), and $nbins$ is the number of histogram bins (40).

Table 3. Computational complexity of the proposed MFI scheme.

Operation	Multipliers	Adders	Comparators
Power normalization	N	$N-1$	0
Generation of amplitude histograms	0	$2 \times nbins$	$2 \times nbins \times N + 2 \times N - 3$
Partition operation	0	$nbins-1$	$10 \times nbins$
Calculation of ratios	$6 \times (nbins + 1)$	$4 \times nbins + 8$	0
Comparing with threshold	0	0	4
Total	$N + 6 \times (nbins + 1)$	$N + 7 \times nbins + 6$	$2 \times N + (2 \times N + 10) \times nbins + 1$

A complexity comparison between the proposed MFI scheme and schemes using DNN, PCASP and M-PSO is shown in Figure 18. Without considering the complexity of power normalization and amplitude histogram generation, in the testing stage of SVM, $O(N_s \cdot d \cdot N)$ operations were required when RBF kernel was applied [38], where N_s , d and N are the number of support vectors, the dimension of the input data and the number of testing

samples, respectively. Since the support vector cannot be fully quantified, the complexity of SVM was not considered, as shown in Figure 18. In the numerical simulations, N_s and d were 805 and 40, respectively. As shown in Figure 18, the required multiplications, additions and comparisons for the M-PSO scheme were much higher than those of the proposed scheme. In addition, 16,000 look-up table (LUT) operations were also required for the M-PSO scheme. When the number of symbols N equaled 2048, the PCASP scheme needed calculations of 131,143 real multiplications, 108,612 real additions, 14 comparisons and 22 LUT operations. For the proposed scheme, the required real multiplications, real additions and comparisons were 6246, 6286 and 492,401, respectively. It should be noted that the complexity of the comparators was much lower than those related to multipliers and adders [29]. The proposed scheme and the scheme using DNN were both based on amplitude histogram. Without considering the complexities of power normalization and amplitude histogram generation, the required real multipliers, real adders and comparators for the identification process in the proposed scheme were $6 \times (nbins + 1)$, $5 \times nbins + 7$ and $10 \times nbins + 4$, respectively. The identification process in DNN, however, required $N_1N_2 + N_2N_3 + N_3N_4 + C-1$ multipliers, $(N_1-1)N_2 + (N_2-1)N_3 + (N_3-1)N_4 + C-1$ adders and $N_2 + N_3 + C-1$ comparators, respectively [6]; here, N_1, N_2, N_3 and N_4 are the numbers of neurons in the input, first hidden, second hidden and output layer, respectively, and C is the number of identified modulation formats. In this paper, N_1, N_2, N_3, N_4 and C were taken to be 40, 40, 10, 5 and 5, respectively. In addition, the training processes for DNN and SVM could also require considerable computational resources and long processing times. Even though the training process could be accomplished offline, the training procedure could still be regarded as a major factor limiting the flexibility of EONs.

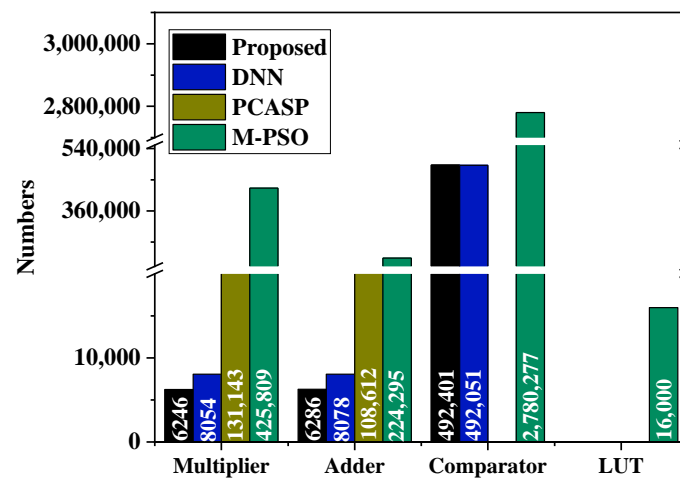


Figure 18. The complexity comparison between the proposed scheme and schemes using DNN, PCASP and M-PSO.

6. Discussion

In Section 3, we discussed the scalability of the proposed scheme. The precondition under which the proposed scheme could still identify PS-QAM would require that the relevant statistical features of the PS-QAM to be identified remain constant. If the information entropy changes, the probability distribution features of PS-QAM will also change. As such, when PS-QAM with different information entropy needs to be identified, corresponding modifications to the procedure of the proposed MFI scheme and their relevant thresholds must be made. The proposed scheme was suitable for application scenarios wherein the set of the modulation formats that need to be identified from are made known before applying the MFI scheme. The authors would like to highlight the fact that such a condition also holds for machine learning MFI algorithms, since they also need training samples to contain the modulation formats to be identified in their training process. In other words, if the modulation formats of an incoming signal are not known before the training process

is applied, the machine learning algorithm will also fail to work properly. Furthermore, the proposed scheme cannot identify higher-order modulation formats, such as 128QAM and 256QAM, because of its low tolerance to noise. Under the influence of noise, the corresponding amplitude features of these higher-order modulation formats will not be highlighted in the histogram, resulting in increased difficulty of identification. Future work will determine methods by which to identify the higher-order modulation formats.

7. Conclusions

In this paper, an MFI scheme, based on amplitude histogram distributions was proposed for use in autonomous digital coherent receivers in EONs. The feasibility of the proposed scheme was verified by numerical simulations for 28 GBaud PDM-QPSK/-8QAM/-16QAM/-32QAM/-64QAM signals over a wide range of OSNRs. Following the numerical simulations, to further demonstrate the effectiveness of the proposed scheme, proof-of-concept experiments were undertaken in 28 GBaud PDM-QPSK/-8QAM/-16QAM, and 21.5 GBaud PDM-32QAM systems under back-to-back and long-haul fiber transmission links. Simulation and experimental results showed that the proposed scheme was robust against both linear and nonlinear noise. Equally importantly, such performances were obtained with significantly reduced complexity. The proposed scheme was dependent on amplitude features only, and was, therefore, insensitive to carrier phase noise. In addition, the proposed MFI scheme was also capable of identifying PS-QAM signals when slight modifications to the procedure and corresponding thresholds were made. According to the tradeoff between the identification performance and computational complexity, the proposed MFI scheme may have good potential for implementation in future EONs.

Author Contributions: Conceptualization, M.H. and X.J.; methodology, M.H., X.J., X.X. and J.T.; software, M.H., X.J. and W.H.; validation, M.H. and X.J.; formal analysis, M.H., X.J. and J.T.; writing—original draft preparation, M.H. and X.J.; writing—review and editing, J.T. and R.G.; supervision, J.T., R.G. and X.X.; project administration, M.H., J.T. and R.G.; funding acquisition, M.H., J.T. and R.G. All authors have read and agreed to the published version of the manuscript.

Funding: This research was partly supported by the Sichuan Science and Technology Program (2023YFH0067), the DSP Centre, funded by the European Regional Development Fund through the Welsh government, and also by the North Wales Growth Deal through Ambition North Wales, the Welsh and UK governments, and the Opening Project of Key Laboratory of Higher Education of Sichuan Province for Enterprise Informationalization and Internet of Things (2021WYJ03).

Institutional Review Board Statement: Not applicable.

Informed Consent Statement: Not applicable.

Data Availability Statement: Data underlying the results presented in this paper are not publicly available at this time but may be obtained from the authors upon reasonable request.

Acknowledgments: This work was supported by the program of China Scholarship Council (No. 202008515061) and the Innovation Fund of Postgraduate, Sichuan University of Science & Engineering (y2021070).

Conflicts of Interest: The authors declare no conflict of interest.

References

1. Gerstel, O.; Jinno, M.; Lord, A.; Yoo, S.B. Elastic optical networking: A new dawn for the optical layer? *IEEE Commun. Mag.* **2012**, *50*, s12–s20. [[CrossRef](#)]
2. Feng, J.; Jiang, L.; Yan, L.; Yi, A.; Pan, W.; Luo, B. Intelligent Optical Performance Monitoring Based on Intensity and Differential-Phase Features for Digital Coherent Receivers. *J. Light. Technol.* **2022**, *40*, 3592–3601. [[CrossRef](#)]
3. Zhao, Y.; Yu, Z.; Wan, Z.; Hu, S.; Shu, L.; Zhang, J.; Xu, K. Low Complexity OSNR Monitoring and Modulation Format Identification Based on Binarized Neural Networks. *J. Light. Technol.* **2020**, *38*, 1314–1322. [[CrossRef](#)]
4. Zhao, L.; Xu, H.; Bai, S.; Bai, C. Modulus mean square-based blind hybrid modulation format recognition for orthogonal frequency division multiplexing-based elastic optical networking. *Opt. Commun.* **2019**, *445*, 284–290. [[CrossRef](#)]

5. Jiang, L.; Yan, L.; Yi, A.; Pan, Y.; Hao, M.; Pan, W.; Luo, B. Blind optical modulation format identification assisted by signal intensity fluctuation for autonomous digital coherent receivers. *Opt. Express* **2020**, *28*, 302–313. [[CrossRef](#)]
6. Zhao, Y.; Shi, C.; Wang, D.; Chen, X.; Wang, L.; Yang, T.; Du, J. Low-Complexity and Nonlinearity-Tolerant Modulation Format Identification Using Random Forest. *IEEE Photon.-Technol. Lett.* **2019**, *31*, 853–856. [[CrossRef](#)]
7. Yang, L.; Xu, H.; Bai, C.; Yu, X.; You, K.; Sun, W.; Guo, J.; Zhang, X.; Liu, C. Modulation Format Identification Using Graph-Based 2D Stokes Plane Analysis for Elastic Optical Network. *IEEE Photon.-J.* **2021**, *13*, 7901315. [[CrossRef](#)]
8. Xu, H.; Yang, L.; Yu, X.; Zheng, Z.; Bai, C.; Sun, W.; Zhang, X. Blind and low-complexity modulation format identification scheme using principal component analysis of Stokes parameters for elastic optical networks. *Opt. Express* **2020**, *28*, 20249–20263. [[CrossRef](#)] [[PubMed](#)]
9. Xiang, M.; Zhuge, Q.; Qiu, M.; Zhou, X.; Zhang, F.; Tang, M.; Liu, D.; Fu, S.; Plant, D.V. Modulation format identification aided hitless flexible coherent transceiver. *Opt. Express* **2016**, *24*, 15642–15655. [[CrossRef](#)] [[PubMed](#)]
10. Xiang, M.; Zhuge, Q.; Qiu, M.; Zhou, X.; Tang, M.; Liu, D.; Fu, S.; Plant, D.V. RF-pilot aided modulation format identification for hitless coherent transceiver. *Opt. Express* **2017**, *25*, 463–471. [[CrossRef](#)] [[PubMed](#)]
11. Fu, S.; Xu, Z.; Lu, J.; Jiang, H.; Wu, Q.; Hu, Z.; Tang, M.; Liu, D.; Chan, C.C.-K. Modulation format identification enabled by the digital frequency-offset loading technique for hitless coherent transceiver. *Opt. Express* **2018**, *26*, 7288–7296. [[CrossRef](#)]
12. Borkowski, R.; Zibar, D.; Caballero, A.; Arlunno, V.; Monroy, I.T. Stokes Space-Based Optical Modulation Format Recognition for Digital Coherent Receivers. *IEEE Photon.-Technol. Lett.* **2013**, *25*, 2129–2132. [[CrossRef](#)]
13. Chen, P.; Liu, J.; Wu, X.; Zhong, K.; Mai, X. Subtraction-Clustering-Based Modulation Format Identification in Stokes Space. *IEEE Photon.-Technol. Lett.* **2017**, *29*, 1439–1442. [[CrossRef](#)]
14. Mai, X.; Liu, J.; Wu, X.; Zhang, Q.; Guo, C.; Yang, Y.; Li, Z. Stokes space modulation format classification based on non-iterative clustering algorithm for coherent optical receivers. *Opt. Express* **2017**, *25*, 2038–2050. [[CrossRef](#)] [[PubMed](#)]
15. Hao, M.; Yan, L.; Yi, A.; Jiang, L.; Pan, Y.; Pan, W.; Luo, B. Stokes Space Modulation Format Identification for Optical Signals Using Probabilistic Neural Network. *IEEE Photon.-J.* **2018**, *10*, 7202213. [[CrossRef](#)]
16. Jiang, L.; Yan, L.; Yi, A.; Pan, Y.; Bo, T.; Hao, M.; Pan, W.; Luo, B. Blind Density-Peak-Based Modulation Format Identification for Elastic Optical Networks. *J. Light. Technol.* **2018**, *36*, 2850–2858. [[CrossRef](#)]
17. Zhang, W.; Zhu, D.; He, Z.; Zhang, N.; Zhang, X.; Zhang, H.; Li, Y. Identifying modulation formats through 2D Stokes planes with deep neural networks. *Opt. Express* **2018**, *26*, 23507–23517. [[CrossRef](#)] [[PubMed](#)]
18. Yi, A.; Yan, L.; Liu, H.; Jiang, L.; Pan, Y.; Luo, B.; Pan, W. Modulation format identification and OSNR monitoring using density distributions in Stokes axes for digital coherent receivers. *Opt. Express* **2019**, *27*, 4471–4479. [[CrossRef](#)] [[PubMed](#)]
19. Cho, H.J.; Varughese, S.; Lippiatt, D.; Desalvo, R.; Tibuleac, S.; Ralph, S.E. Optical performance monitoring using digital coherent receivers and convolutional neural networks. *Opt. Express* **2020**, *28*, 32087–32104. [[CrossRef](#)]
20. Yu, X.; Bai, C.; Xu, H.; Sun, W.; Yang, L.; Zheng, H.; Hu, W. A modified PSO assisted blind modulation format identification scheme for elastic optical networks. *Opt. Commun.* **2020**, *476*, 126280. [[CrossRef](#)]
21. Wang, M.; Liu, J.; Zhang, J.; Zhang, D.; Guo, C. Modulation format identification based on phase statistics in Stokes space. *Opt. Commun.* **2021**, *480*, 126481. [[CrossRef](#)]
22. Xiang, Q.; Yang, Y.; Zhang, Q.; Yao, Y. Joint, accurate and robust optical signal-to-noise ratio and modulation format monitoring scheme using a single Stokes-parameter-based artificial neural network. *Opt. Express* **2021**, *29*, 7276–7287. [[CrossRef](#)]
23. Zhao, R.; Sun, W.; Xu, H.; Bai, C.; Tang, X.; Wang, Z.; Yang, L.; Cao, L.; Bi, Y.; Yu, X.; et al. Blind modulation format identification based on improved PSO clustering in a 2D Stokes plane. *Appl. Opt.* **2021**, *60*, 9933–9942. [[CrossRef](#)]
24. Liu, J.; Dong, Z.; Zhong, K.P.; Lau, A.P.T.; Lu, C.; Lu, Y. Modulation Format Identification Based on Received Signal Power Distributions for Digital Coherent Receivers. In Proceedings of the Optical Fiber Communication Conference, (Optical Society of America), San Francisco, CA, USA, 9–13 March 2014; pp. 1–3. [[CrossRef](#)]
25. Bilal, S.M.; Bosco, G.; Dong, Z.; Lau, P.T.A.; Lu, C. Blind modulation format identification for digital coherent receivers. *Opt. Express* **2015**, *23*, 26769–26778. [[CrossRef](#)] [[PubMed](#)]
26. Lin, X.; Eldemerdash, Y.A.; Dobre, O.A.; Zhang, S.; Li, C. Modulation Classification Using Received Signal's Amplitude Distribution for Coherent Receivers. *IEEE Photon.-Technol. Lett.* **2017**, *29*, 1872–1875. [[CrossRef](#)]
27. Liu, G.; Proietti, R.; Zhang, K.; Lu, H.; Yoo, S.B. Blind modulation format identification using nonlinear power transformation. *Opt. Express* **2017**, *25*, 30895–30904. [[CrossRef](#)] [[PubMed](#)]
28. Jiang, L.; Yan, L.; Yi, A.; Pan, Y.; Hao, M.; Pan, W.; Luo, B. An Effective Modulation Format Identification Based on Intensity Profile Features for Digital Coherent Receivers. *J. Light. Technol.* **2019**, *37*, 5067–5075. [[CrossRef](#)]
29. Lu, J.; Tan, Z.; Lau, A.P.T.; Fu, S.; Tang, M.; Lu, C. Modulation format identification assisted by sparse-fast-Fourier-transform for hitless flexible coherent transceivers. *Opt. Express* **2019**, *27*, 7072–7086. [[CrossRef](#)]
30. Zhao, Z.; Yang, A.; Guo, P. A Modulation Format Identification Method Based on Information Entropy Analysis of Received Optical Communication Signal. *IEEE Access* **2019**, *7*, 41492–41497. [[CrossRef](#)]
31. Zhao, Z.; Yang, A.; Guo, P.; Tan, Q.; Xin, X. A modulation format identification method based signal amplitude sorting and ratio calculation. *Opt. Commun.* **2020**, *470*, 125819. [[CrossRef](#)]
32. Yang, L.; Xu, H.; Bai, C.; Yu, X.; You, K.; Sun, W.; Zhang, X.; Liu, C. Low-complexity modulation format identification scheme via graph-theory in digital coherent optical receivers. *Opt. Commun.* **2021**, *501*, 127380. [[CrossRef](#)]

33. Yang, L.; Xu, H.; Bai, C.; Yu, X.; Ge, P.; You, K.; Sun, W.; Zhang, X.; Liu, C. Joint modulation format identification and OSNR estimation method based on trajectory information analysis. *Opt. Commun.* **2022**, *507*, 127657. [[CrossRef](#)]
34. Khan, F.N.; Zhong, K.; Al-Arashi, W.H.; Yu, C.; Lu, C.; Lau, A.P.T. Modulation Format Identification in Coherent Receivers Using Deep Machine Learning. *IEEE Photon.-Technol. Lett.* **2016**, *28*, 1886–1889. [[CrossRef](#)]
35. Khan, F.N.; Zhong, K.; Zhou, X.; Al-Arashi, W.H.; Yu, C.; Lu, C.; Lau, A.P.T. Joint OSNR monitoring and modulation format identification in digital coherent receivers using deep neural networks. *Opt. Express* **2017**, *25*, 17767–17776. [[CrossRef](#)]
36. Wang, T.; Liu, X. A novel modulation format identification based on amplitude histogram space. *Front. Optoelectron.* **2019**, *12*, 190–196. [[CrossRef](#)]
37. Zhu, C.; Tran, A.V.; Chen, S.; Du, L.B.; Do, C.C.; Anderson, T.; Lowery, A.; Skafidas, E. Statistical moments-based OSNR monitoring for coherent optical systems. *Opt. Express* **2012**, *20*, 17711–17721. [[CrossRef](#)] [[PubMed](#)]
38. Lin, X.; Dobre, O.A.; Ngatched, T.M.N.; Eldemerdash, Y.A.; Li, C. Joint Modulation Classification and OSNR Estimation Enabled by Support Vector Machine. *IEEE Photon.-Technol. Lett.* **2018**, *30*, 2127–2130. [[CrossRef](#)]

Disclaimer/Publisher’s Note: The statements, opinions and data contained in all publications are solely those of the individual author(s) and contributor(s) and not of MDPI and/or the editor(s). MDPI and/or the editor(s) disclaim responsibility for any injury to people or property resulting from any ideas, methods, instructions or products referred to in the content.